

# Unconventional thermal metallic state of charge-neutral fermions in an insulator

Y. Sato<sup>1</sup>, Z. Xiang<sup>2</sup>, Y. Kasahara<sup>1</sup>, T. Taniguchi<sup>1</sup>, S. Kasahara<sup>1</sup>, L. Chen<sup>2</sup>, T. Asaba<sup>2,3</sup>, C. Tinsman<sup>2</sup>, H. Murayama<sup>1</sup>, O. Tanaka<sup>4</sup>, Y. Mizukami<sup>4</sup>, T. Shibauchi<sup>4</sup>, F. Iga<sup>5</sup>, J. Singleton<sup>6</sup>, Lu Li<sup>2\*</sup> and Y. Matsuda<sup>1\*</sup>

**Quantum oscillations in transport and thermodynamic parameters at high magnetic fields are an unambiguous signature of the Fermi surface, the defining characteristic of a metal. Recent observations of quantum oscillations in insulating SmB<sub>6</sub> and YbB<sub>12</sub>, therefore, have been a big surprise—despite the large charge gap inferred from the insulating behaviour of the resistivity, these compounds seemingly host a Fermi surface at high magnetic fields. However, the nature of the ground state in zero field has been little explored. Here, we report the use of low-temperature heat-transport measurements to discover gapless, itinerant, charge-neutral excitations in the ground state of YbB<sub>12</sub>. At zero field, sizeable linear temperature-dependent terms in the heat capacity and thermal conductivity are clearly resolved in the zero-temperature limit, indicating the presence of gapless fermionic excitations with an itinerant character. Remarkably, linear temperature-dependent thermal conductivity leads to a spectacular violation of the Wiedemann-Franz law: the Lorenz ratio is 10<sup>4</sup>–10<sup>5</sup> times larger than that expected in conventional metals, indicating that YbB<sub>12</sub> is a charge insulator and a thermal metal. Moreover, we find that these fermions couple to magnetic fields, despite their charge neutrality. Our findings expose novel quasiparticles in this unconventional quantum state.**

In intermetallic *4f* and *5f* compounds, strong hybridization between itinerant and predominately localized electrons often opens an insulating gap<sup>1,2</sup>. Among such Kondo insulators, SmB<sub>6</sub> and YbB<sub>12</sub> have recently aroused great interest due to several remarkable properties. Theoretical works suggest that both are topologically non-trivial<sup>3,4</sup>, and that they possess three-dimensional (3D) insulating bulk states and metallic 2D surfaces. The surface states in SmB<sub>6</sub> are protected by time-reversal and inversion symmetries, while those in YbB<sub>12</sub> are protected by crystal symmetry. In both compounds, the metallic surface states have been established using a number of experimental techniques, including angle-resolved photoemission spectroscopy<sup>5,6</sup>. In particular, in SmB<sub>6</sub>, spin-resolved angle-resolved photoemission spectroscopy has shown the spin-momentum-locked surface, which is a characteristic feature of a topological insulator.

Recently, another salient aspect of both compounds has come as a great surprise. In an external magnetic field, SmB<sub>6</sub> exhibits quantum oscillations (QOs) in magnetization (the de Haas–van Alphen (dHvA) effect), which is associated with Landau quantization<sup>7–10</sup>. However, it is still unclear whether the dHvA signal in SmB<sub>6</sub> results from the metallic surface or insulating bulk states. It has been pointed out theoretically that QOs in magnetization can indeed occur in a certain type of band insulator via magnetic breakdown in strong magnetic fields<sup>11–13</sup>. Even more exotic possibilities have been suggested, such as neutral fermions that form a Fermi surface<sup>14–17</sup> or non-Hermitian Landau quantization of the in-gap states<sup>18,19</sup>. Following these scenarios, unusual quasiparticles, such as composite excitons and neutral Majorana fermions, have been proposed. If these charge-neutral degrees of freedom form structures similar to the Fermi surface of metals, they may well produce dHvA oscillations.

The linear temperature dependence of the heat capacity  $C$  and thermal conductivity  $\kappa_{xx}$  at low temperatures indicates the presence of gapless fermion-like excitations. Their observations are therefore a natural consequence of a Fermi surface. As the heat capacity includes both localized and itinerant excitations, a finite linear heat capacity coefficient  $\gamma$  does not always indicate the presence of mobile gapless excitations. In fact, amorphous solids and spin glasses exhibit a finite  $\gamma$ , although the excitations in these systems are localized<sup>20</sup>. Moreover, the Schottky contribution to the heat capacity often prevents the detailed analysis of  $C$  at low temperatures. On the other hand,  $\kappa_{xx}$  is determined exclusively by itinerant excitations<sup>21</sup>. As the Schottky contribution arises from localized excitations, it cannot carry heat. Thus,  $\kappa_{xx}$  is free from the Schottky contribution, enabling us to extend the measurements down to lower temperatures. The finite  $\kappa_{xx}^0/T$ , therefore, provides the most direct and compelling evidence for the presence of the itinerant and gapless fermionic excitations, analogous to the excitations near the Fermi surface in pure metals<sup>21</sup>. In SmB<sub>6</sub>, although a finite  $\gamma$  is observed<sup>8</sup>, there is no term in the zero-field thermal conductivity that is linear in  $T$  (that is,  $\kappa_{xx}^0/T=0$ )<sup>9,22,23</sup>. This suggests that itinerant gapless neutral fermions are absent in zero field. There has been intense debate as to whether such fermions are excited by magnetic field; while field-induced enhancement of the thermal conductivity has been attributed to excitations of neutral fermions<sup>9</sup>, an alternative interpretation involving conventional phonon mechanisms has been pointed out<sup>23</sup>. In addition, neutron inelastic scattering experiments reveal distinct excitation modes within the hybridization gap<sup>24</sup>, but there is no evidence of charge-neutral excitations. Whether or not there are non-trivial itinerant quasiparticles, which

<sup>1</sup>Department of Physics, Kyoto University, Kyoto, Japan. <sup>2</sup>Department of Physics, University of Michigan, Ann Arbor, MI, USA. <sup>3</sup>MPA-CMMS, Los Alamos National Laboratory, Los Alamos, NM, USA. <sup>4</sup>Department of Advanced Materials Science, University of Tokyo, Chiba, Japan. <sup>5</sup>Institute of Quantum Beam Science, Graduate School of Science and Engineering, Ibaraki University, Mito, Japan. <sup>6</sup>Los Alamos National Laboratory, Los Alamos, NM, USA.

\*e-mail: [luli@umich.edu](mailto:luli@umich.edu); [matsuda@scphys.kyoto-u.ac.jp](mailto:matsuda@scphys.kyoto-u.ac.jp)

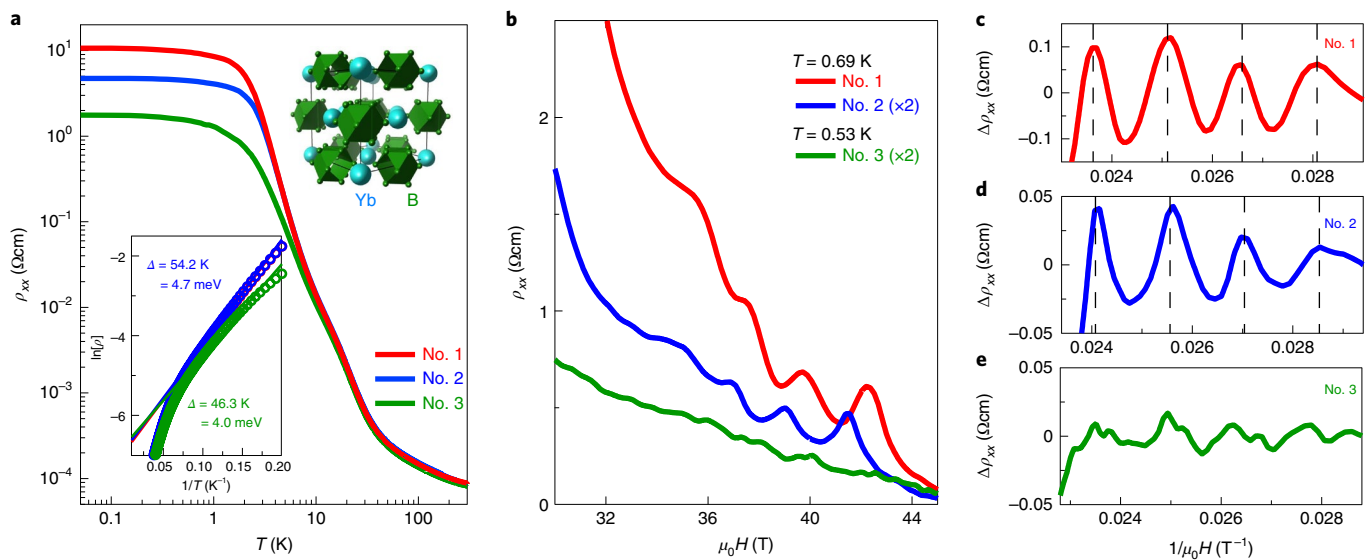


**Fig. 1 | The resistivity of  $\text{YbB}_{12}$ .** **a**, The temperature dependence of the resistivity in three crystals (crystals 1 and 2 from the same batch and crystal 3 from another batch) of  $\text{YbB}_{12}$ . The bottom left inset is an Arrhenius plot above 5 K. Also shown (top right inset) is the crystal structure;  $\text{YbB}_{12}$  crystallizes in the face-centred cubic  $\text{UB}_{12}$ -type structure, in which strongly covalently bonded units of  $\text{B}_{12}$  cuboctahedra form a cubic lattice and interstitial Yb atoms are accommodated in the octahedral pores among these units. **b**, The field dependence of the resistivity at high magnetic fields applied close to the  $c$  axis for 0.69 K for crystals 1 and 2 and 0.53 K for crystal 3. **c–e**, The oscillatory part of the magnetoresistance plotted against the inverse field in crystals 1 (**c**), 2 (**d**) and 3 (**e**). The oscillatory components are obtained by subtracting a fifth-order polynomial background from the raw data shown in **b**. In **c** and **d**, the dashed lines mark the evenly spaced peaks of the SdH oscillations.

may be responsible for the observed dHvA oscillations, therefore remains a controversial issue in the case of  $\text{SmB}_6$ .

The very recent discovery of resistivity QOs (the Shubnikov–de Haas (SdH) effect, which is absent in  $\text{SmB}_6$ ) in another Kondo insulator,  $\text{YbB}_{12}$ , has revealed a novel aspect of the QOs in insulators<sup>25</sup>. In  $\text{YbB}_{12}$ ,  $4f$  and  $5d$  band hybridization leads to a narrow insulating gap, which has been confirmed directly by a variety of spectroscopic experiments, including inelastic neutron scattering<sup>26</sup>, photoemission spectroscopy<sup>27</sup> and nuclear magnetic resonance<sup>28</sup>. The mean valence of the Yb ions is close to +3 ( $4f^{13}$  state)<sup>29</sup>. Compared to the situation in the mixed-valence compound  $\text{SmB}_6$  (ref. 30), this suggests a simpler electronic state in  $\text{YbB}_{12}$ , with the  $f$  electrons mostly localized.

The 3D nature of the SdH signal in  $\text{YbB}_{12}$  demonstrates that the QOs in the resistivity arise from the electrically insulating bulk. We note that the possibility of SdH oscillations arising from metallic domains induced by impurities or strain, or from a minority portion of the sample is ruled out on the basis of the symmetry analysis and simulations<sup>25</sup>. In addition, the QOs in  $\text{YbB}_{12}$  behave in other ways that are different from those in  $\text{SmB}_6$ . In  $\text{SmB}_6$ , the effective masses  $m^*$  of the quasiparticles determined from dHvA oscillations are much smaller than the free-electron mass  $m_e$ , indicating that correlation effects are of little importance. Moreover, the temperature dependences of the QO amplitudes in some  $\text{SmB}_6$  crystals deviate strikingly from the predictions of the standard Lifshitz–Kosevich formula applicable to Fermi liquids at very low temperatures<sup>31,32</sup>. By contrast, in  $\text{YbB}_{12}$ , the  $m^*$  values estimated from SdH oscillations are much larger than  $m_e$ , implying strong correlation effects. Moreover, the oscillations accurately obey the Lifshitz–Kosevich formula, showing no deviation from Fermi-liquid theory<sup>25</sup>.

Figure 1a depicts the  $T$  dependence of the resistivity  $\rho_{xx}$  for three different crystals (crystals 1 and 2 are taken from the same batch and 3 is from a different batch) grown by the floating-zone technique. In all crystals,  $\rho_{xx}$  increases by 4–5 orders of magnitude from room temperature to 0.1 K. Below  $T \approx 2$  K,  $\rho_{xx}$  becomes weakly temperature dependent, resembling the  $T < 3.5$  K resistive ‘plateau’ well known in  $\text{SmB}_6$  (ref. 31); this ‘plateau’ is attributed to the metallic

surface state. The residual resistivities  $\rho_{xx}^0$  are approximately 11, 4.5 and 1.8  $\Omega\text{cm}$  for crystals 1, 2 and 3, respectively. The inset of Fig. 1a shows an Arrhenius plot of  $\rho_{xx}$  above 5 K, where the surface conduction is negligible. Obviously, the  $\rho_{xx}$  plots of all crystals show an activation-type temperature dependence with two-gap behaviour. The resistivities of crystals 1 and 2 overlap above 5 K, while that of crystal 3 is lower than those of crystals 1 and 2 below  $\sim 20$  K. Fitting with a thermal activation model of the resistivity ( $\rho_{xx}(T) \propto \exp(\Delta/2k_B T)$ ), we obtain gap widths of 4.7 meV for crystals 1 and 2 and 4.0 meV for crystal 3 over the temperature range 6 K  $< T < 12.5$  K. Despite their similar activation energies,  $\rho_{xx}^0$  of crystal 1 is 2.2 times larger than that of crystal 2 at the lowest temperatures. This is consistent with the presence of the 2D metallic surface. In fact, assuming the same surface conductance of both crystals,  $\rho_{xx}^0$  is reduced in the thinner crystal as expected, because the surface-to-volume ratio increases with reduced sample thickness (see Supplementary Fig. 1 and Methods).

Figure 1b depicts the field dependence of the resistivity  $\rho_{xx}(H)$  at 0.69 K for crystals 1 and 2 and at 0.53 K for crystal 3 with the magnetic field applied close to the  $c$  axis. On applying field, the negative slope of the  $\rho_{xx}(T)$  curve, an indication of the field-induced gap-closing process<sup>25,32</sup>, is preserved up to 45 T with no signature of metallic behaviour. Figure 1c–e displays the oscillatory part of the resistivity  $\Delta\rho_{xx}$ , which is obtained by subtracting a polynomial background from  $\rho_{xx}(H)$ , plotted as a function of  $1/\mu_0 H$ . For crystals 1 and 2, four periods with an approximately constant spacing provide strong evidence that these are SdH oscillations. A direct quantitative comparison of the carrier scattering rate between crystals 1 and 2 is difficult due to the different surface contributions, but the fact that the oscillations start above approximately 33 T in both crystals suggests similar scattering rates, which is consistent with the samples possessing the same activation energy. For crystal 3, on the other hand, no discernible oscillations are observed (Fig. 1b,e), suggesting a larger scattering rate. In insulators, a large activation energy usually indicates a low impurity concentration and high crystallographic quality. From this point of view, the quality of crystals 1 and 2 is similar, and better

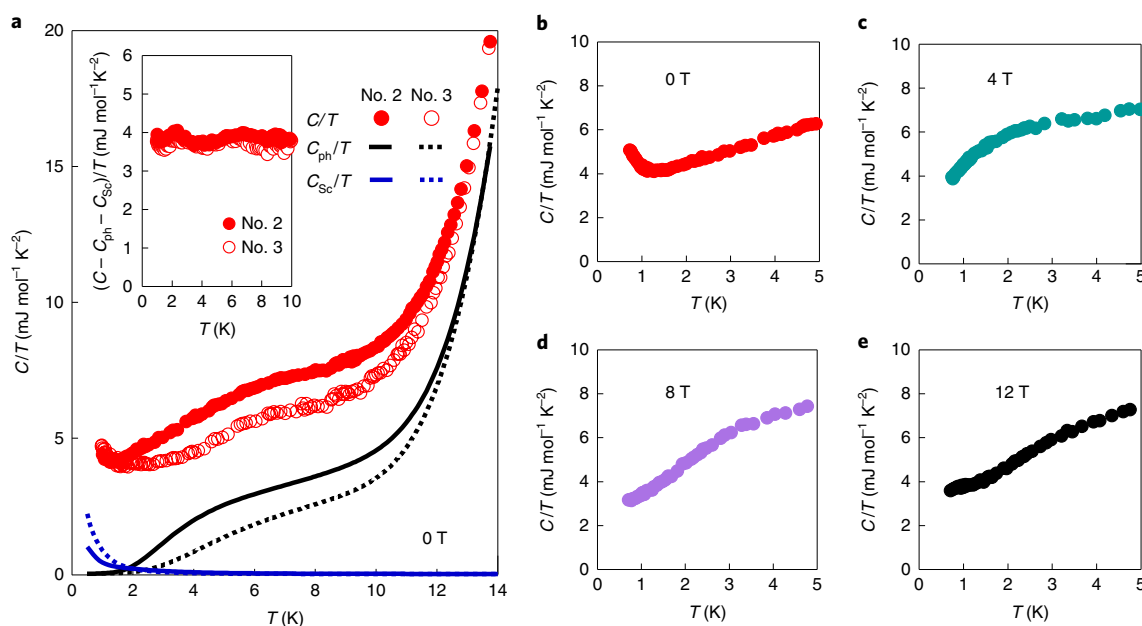


**Fig. 2 | The heat capacity of  $\text{YbB}_{12}$ .** **a**, The temperature dependence of the heat capacity divided by the temperature  $C/T$  in zero field for crystals 2 and 3. The black solid and dotted lines represent the phonon heat capacity obtained by the Debye and Einstein contributions (see Methods) for crystals 2 and 3, respectively. The best fit is obtained by  $\beta = 0.026 \text{ mJ mol}^{-1} \text{K}^{-4}$  and two Einstein modes with  $\theta_E = 16 \text{ K}$  and  $170 \text{ K}$  for crystal 2 and  $\beta = 0.017 \text{ mJ mol}^{-1} \text{K}^{-4}$  and  $\theta_E = 24 \text{ K}$  and  $160 \text{ K}$  for crystal 3. The blue solid and dotted lines represent the Schottky contributions obtained by the three-level model (see Methods), with  $\Delta_1 = 1.4 \text{ K}$  and  $\Delta_2 = 6.2 \text{ K}$ , and  $\Delta_1 = 0.6 \text{ K}$  and  $\Delta_2 = 2.2 \text{ K}$  for crystals 2 and 3, respectively. The inset shows the quasiparticle contribution  $C_{\text{qp}}/T$ , which is obtained by subtracting the Schottky and phonon contributions from the total heat capacity. **b–e**,  $C/T$  of crystal 2 at low temperatures in zero field (**b**) and in magnetic fields applied along the  $[1,0,0]$  direction (**c–e**).

than that of crystal 3 with its lower activation energy. Thus, remarkably, the more insulating crystals exhibit larger SdH oscillations, the opposite of the behaviour of conventional metals.

Figure 2a depicts the temperature dependence of the heat capacity divided by the temperature ( $C/T$ ) of crystals 2 and 3 in zero field. As shown in Fig. 2b,  $C/T$  shows a slight upturn below  $\sim 1 \text{ K}$ , which is attributed to a Schottky contribution  $C_{\text{Sc}}/T$ . Despite this, it is obvious that an extrapolation of  $C/T$  from above  $1 \text{ K}$  to  $T=0$  has a finite intercept, indicating the presence of a linear temperature term; that is, the gapless quasiparticle excitations possess  $C_{\text{qp}} = \gamma T$ . Thus, the heat capacity can be written as a sum of the phonon, quasiparticle and Schottky contributions,  $C = C_{\text{ph}} + C_{\text{qp}} + C_{\text{Sc}}$ . The low-temperature enhancement of  $C/T$  is well fitted by a three-level Schottky model, as shown by the blue solid and dotted lines in Fig. 2a. In cubic  $\text{YbB}_{12}$ , 3D phonon dispersions have been revealed by inelastic neutron scattering experiments<sup>33</sup>. As reported in the isostructural compounds  $\text{LuB}_{12}$  and  $\text{YB}_{12}$ , a hump anomaly around  $6 \text{ K}$  and steep increase above  $10 \text{ K}$  in  $C/T$  may be attributed to low-energy optical phonon modes of Yb atoms in the cavities of the  $\text{B}_{24}$  cuboctahedrons<sup>34</sup>. The solid and dotted black lines indicate  $C_{\text{ph}}/T$ , which includes contributions from both the acoustic phonon ( $\propto T^3$ ) and two optical phonon modes. The optical phonon contributions are slightly sample dependent. Owing to the high Debye temperature, the acoustic phonon contribution to the total heat capacity is very small. As shown in the inset of Fig. 2a,  $C_{\text{qp}}/T$  (obtained by subtracting  $C_{\text{ph}}$  and  $C_{\text{Sc}}$  from the total  $C$ ) is in good agreement for crystals 2 and 3. Thus, we obtain  $\gamma \approx 3.8 \text{ mJ mol}^{-1} \text{K}^{-2}$  in zero field, which is comparable to values in conventional metals. As the volume fraction of the impurity phases in the present crystals is estimated to be much less than 1% from the high-resolution synchrotron X-ray diffraction measurements<sup>25</sup>, we can rule out the possibility that the finite  $\gamma$  arises from impurity phases. Figure 2c–e shows  $C/T$  in magnetic field. At  $\mu_0 H = 4 \text{ T}$ ,  $C/T$  decreases with decreasing  $T$  with a downward curvature below  $2 \text{ K}$ . At  $\mu_0 H = 8$  and  $12 \text{ T}$ ,  $C/T$  decreases

nearly linearly with  $T$  with a steeper slope than that of the zero-field data. This low-temperature behaviour may be attributed to the coupling between the magnetic field and the optical phonons; however, a quantitative estimation is difficult. Nevertheless, it is obvious that a simple extrapolation of  $C/T$  to  $T=0$  indicates that  $\gamma$  is slightly reduced by magnetic field.

We now turn to the thermal conductivity that shows the itinerant aspect of the neutral excitations. The filled and open red circles in the inset of Fig. 3a depict the  $T$  dependence of  $\kappa_{xx}/T$  below  $0.3 \text{ K}$  in zero field for crystals 1 and 3, respectively. As the thermal conductivity does not contain the localized Schottky contribution,  $\kappa_{xx}$  can be described as a sum of the itinerant quasiparticle and phonon contributions,  $\kappa_{xx} = \kappa_{xx}^{\text{qp}} + \kappa_{xx}^{\text{ph}}$ . To use  $\kappa_{xx}$  as a probe of itinerant quasiparticles,  $\kappa_{xx}^{\text{ph}}$  must be extracted reliably. Figure 3a depicts  $\kappa_{xx}/T$  plotted as a function of  $T^2$ , revealing that  $\kappa_{xx}/T = \kappa_{xx}^0/T + AT^2$  at low temperatures. The  $AT^2$  term is attributable to phonons for the following reasons. The optical phonon modes are negligible at temperatures well below the Einstein temperature (which is  $16\text{--}24 \text{ K}$  in our samples) because of the small population of optical phonons and the low phonon group velocity. Consequently, acoustic phonons are the only carriers of heat at low temperature and the phonon thermal conductivity is given by  $\kappa_{xx}^{\text{ph}} = \frac{1}{3} \beta T^3 v_{\text{ph}} \ell_{\text{ph}}$ , where  $v_{\text{ph}}$  and  $\ell_{\text{ph}}$  are the sound velocity and mean free path of acoustic phonons, respectively. We compare  $\ell_{\text{ph}}$  and the effective diameter of the sample  $d_{\text{eff}} = 2\sqrt{wt/\pi}$  ( $w$  and  $t$  are the width and thickness of the crystal, respectively);  $d_{\text{eff}} = 0.58 \text{ mm}$  and  $0.37 \text{ mm}$  for crystals 1 and 3, respectively. Using  $\beta = 0.026$  and  $0.017 \text{ mJ mol}^{-1} \text{K}^{-4}$  for crystals 1 and 3, respectively (obtained from the measurements shown in Fig. 2a), and  $v_{\text{ph}} = 9.6 \times 10^3 \text{ m s}^{-1}$  for  $\text{LuB}_{12}$  (ref. 35), we find that  $\ell_{\text{ph}} \approx d_{\text{eff}}$  at  $\sim 0.5 \text{ K}$  for crystal 1 and  $\sim 0.6 \text{ K}$  for crystal 3. These temperatures are close to the temperatures below which  $\kappa_{xx}/T$  shows  $T^2$  dependence, as shown in the inset of Fig. 3a, supporting the above estimation. These results suggest that at low enough temperatures ( $T^2 \lesssim 0.1 \text{ K}^2$ ),  $\ell_{\text{ph}}$  will be limited by the crystal size; that is, the

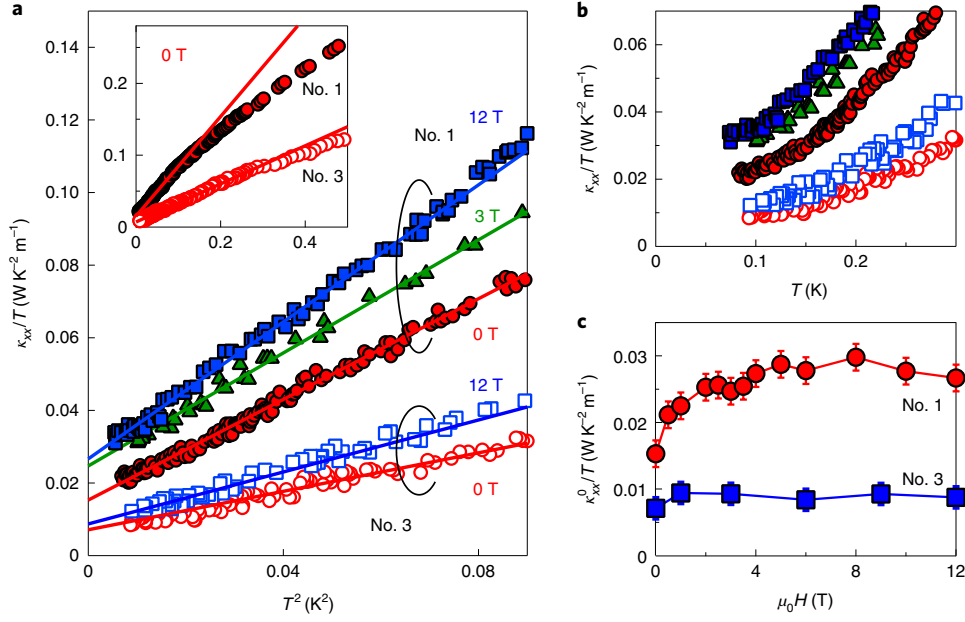


**Fig. 3 | The thermal conductivity of YbB<sub>12</sub>.** **a**, The thermal conductivity divided by the temperature  $\kappa_{xx}/T$  plotted as a function of  $T^2$  in zero field and at  $\mu_0 H = 3$  and 12 T for crystals 1 and 3 at low temperatures. The solid lines represent  $\kappa_{xx}/T = \kappa_{xx}^0/T + AT^2$  obtained by the fitting. The inset shows the same data up to  $T^2 = 0.5 \text{ K}^2$  in zero field. The deviation from the fitting occurs at  $\sim 0.4 \text{ K}$  for crystal 1 and  $\sim 0.5 \text{ K}$  for crystal 3. **b**, The same data plotted as a function of  $T$ . **c**, The field dependence of the residual linear thermal conductivity term  $\kappa_{xx}^0/T$  obtained by the extrapolation to zero temperature at each field. The error bars represent one standard deviation.

samples are in the boundary scattering regime where  $\kappa_{xx}^{\text{ph}}/T \propto T^2$ . The fact that the systems are in this regime is also supported by the  $A$  values of crystals 1 and 3. In the boundary scattering regime,  $A$  is proportional to  $\beta d_{\text{eff}}$ . The ratio of the  $A$  values of crystals 1 and 3 determined by the  $T$  dependence of  $\kappa_{xx}/T$  is  $\sim 2.6$ . This value is close to the ratio ( $\sim 2.5$ ) of  $\beta d_{\text{eff}}$  of the two crystals, indicating the proportionality of  $A$  and  $\beta d_{\text{eff}}$ .

As revealed by both plots of Fig. 3a,b,  $\kappa_{xx}/T$  extrapolated to zero temperature yields definite non-zero intercepts in both crystals,  $\kappa_{xx}^0/T \neq 0$ . Thus, our results provide evidence of a finite residual linear term in  $\kappa_{xx}^{\text{qp}}$  (that is, the presence of itinerant gapless fermionic excitations). We stress that the finite  $\kappa_{xx}^0/T$  is not caused by phonons (see Methods). It is known that localized vibrational modes, such as tunnelling states in amorphous solids, can contribute to a finite  $\gamma$  (ref.<sup>20</sup>). However, such excitations are localized and do not carry heat, resulting in the absence of  $\kappa_{xx}^0/T$ . Moreover, these vibrational modes may act as scattering centres for phonons. This gives a  $T^{-1}$  dependence of  $\ell_{\text{ph}}$ , leading to  $\kappa_{xx} \propto T^2$ , in contrast to the observed non-zero  $\kappa_{xx}^0/T$ . It should also be stressed that the observed finite  $\kappa_{xx}^0/T$  does not originate from charged quasiparticles, in contrast to the situation in conventional metals. Evidence for this is given by the spectacular violation of the Wiedemann-Franz (WF) law, which connects the electronic thermal conductivity  $\kappa_{xx}^e$  to the electrical resistivity. In moderately pure metals at low temperatures,  $L = \kappa_{xx}^e \rho_{xx} / T \leq L_0$  is generally satisfied, where  $L_0 = \frac{\pi^2}{3} \left( \frac{k_B}{e} \right)^2 = 2.44 \times 10^{-8} \text{ W}\Omega \text{ K}^{-2}$  is the Lorenz number<sup>36</sup>. The values of  $\kappa_{xx}^0/T$  for crystals 1 and 3 are found to be  $\sim 6 \times 10^4 L_0$  and  $\sim 5 \times 10^3 L_0$ , respectively. It is highly unlikely that the surface metallic region significantly violates the WF law. In fact, it is well established that the WF law holds in the 2D metals, even in the quantum Hall regime. The WF expectation of  $\kappa_{xx}^0/T$  from the metallic surface is less than  $10^{-4} \text{ W K}^{-2} \text{ m}^{-1}$ , which is by far smaller than the experimental resolution. These results lead us to conclude that the neutral

fermions in the insulating bulk of the samples are responsible for the finite  $\kappa_{xx}^0/T$ . In other words, as the bulk resistivity diverges as  $T \rightarrow 0$ , the Lorenz number for the heat-carrying quasiparticles also diverges. Thus, the thermal conductivity and heat capacity data very strongly suggest the presence of highly mobile and gapless neutral fermion excitations in zero field, which are not observed in SmB<sub>6</sub>.

Finite values of both  $\gamma$  and  $\kappa_{xx}^0/T$  in the insulating state have been reported in a quantum-spin-liquid candidate, the organic compound EtMe<sub>3</sub>Sb[Pd(dmit)<sub>2</sub>]<sub>2</sub> (DMIT) with a 2D triangular lattice<sup>37,38</sup>. In DMIT, finite  $\gamma$  and  $\kappa_{xx}^0/T$  have been discussed in terms of electrically neutral spinons forming the Fermi surface. In addition, in DMIT, a  $T$ -independent Pauli-paramagnetic-like magnetic susceptibility  $\chi$  is observed and the Wilson ratio  $R_W = \frac{4}{3} \left( \frac{\pi k_B}{g\mu_B} \right)^2 \frac{\chi}{\gamma}$  is close to unity, which is a basic property of metals<sup>39</sup>. Temperature-independent  $\chi$  is also observed in YbB<sub>12</sub> (see Supplementary Fig. 5 and Methods) and it may be ascribed to the van Vleck contribution within the  $J = \frac{7}{2}$  multiplet, although there is no quantitative estimation of this contribution. An alternative explanation is that the neutral fermions give rise to Pauli-paramagnetic-like  $\chi$ . A simple estimation of  $R_W$  using the measured  $\chi \approx 3 \times 10^{-3} \text{ emu mol}^{-1}$  and  $\gamma \approx 4 \text{ mJ mol}^{-1} \text{ K}^{-2}$  gives  $R_W \approx 100$ , which is comparable to that reported in some spin-liquid systems<sup>40</sup>. In DMIT, the quantum oscillations have not been observed up to 32 T, although its possible observation is suggested theoretically<sup>41</sup>. Thus, more experiments are needed for quantitative comparisons between these two extraordinary systems.

We note that  $\kappa_{xx}^0/T$  for crystal 1 is nearly twice as large as that for crystal 3, while  $\gamma$  for crystal 2, whose quality is very close to that of crystal 1, coincides with that for crystal 3. The quasiparticle thermal conductivity is related to the heat capacity by

$$\frac{\kappa_{xx}^{\text{qp}}}{T} = \frac{1}{3} \gamma v_F \ell_{\text{qp}} \quad (1)$$

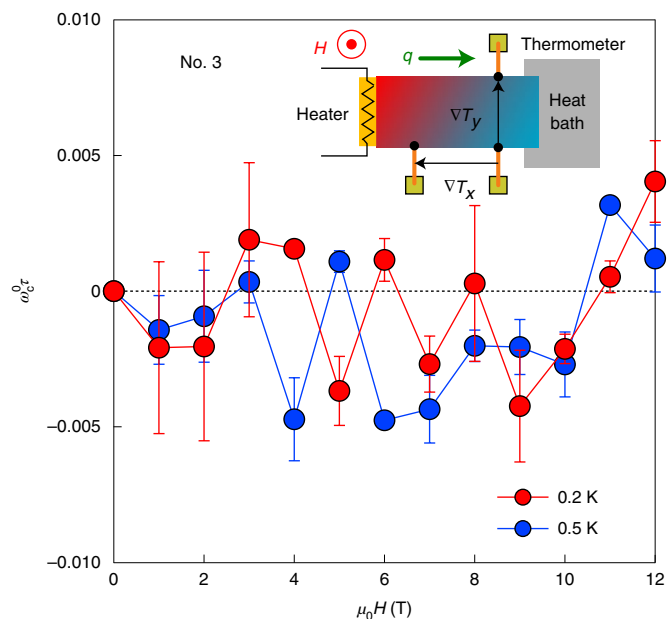


**Fig. 4 | The thermal Hall angle of YbB<sub>12</sub>.** The field dependence of the thermal Hall angle  $\omega_c^0 \tau \equiv \kappa_{xy}^0 / \kappa_{xx}^0$  at 0.2 and 0.5 K. As  $\kappa_{xx} > \kappa_{xx}^0$ ,  $\omega_c \tau$  is smaller than  $\omega_c^0 \tau$ . The error bars represent one standard deviation. The inset illustrates the experimental set-up.

where  $v_F$  is the Fermi velocity and  $\ell_{qp}$  is the mean free path of the neutral fermions. Therefore,  $\ell_{qp}$  of crystals 1 and 2 is twice as large as that of crystal 3. Interestingly, this indicates that more insulating crystals with larger activation energies have higher mobility neutral quasiparticles, supporting the assertion made above when discussing the QOs.

As shown in Fig. 3a,  $\kappa_{xx}/T$  is greatly enhanced by applying magnetic field. More importantly, as depicted in Fig. 3c,  $\kappa_{xx}^0/T$ , which is obtained by extrapolating  $\kappa_{xx}/T$  to zero temperature at each field, is enhanced by field. It should be kept in mind that  $\kappa_{xx}^0/T$  contains no phonon contribution. Therefore, the field-induced enhancement of  $\kappa_{xx}^0/T$  implies that the neutral fermions couple to magnetic fields. Another prominent feature is that  $\kappa_{xx}^0/T$  of crystal 1 is much more enhanced by magnetic field than that of crystal 3, indicating that better quality crystals with lower impurity scattering rates exhibit larger magneto-thermal conductivity. As larger  $\kappa_{xx}^0/T$  values arise from longer mean free paths, this result suggests (as might be expected) that the more mobile neutral fermions are more strongly influenced by magnetic field.

A fascinating question is whether the charge-neutral fermions are responsible for the QOs. To examine this, we estimate  $\ell_{qp}$  from equation (1) by assuming that  $v_F$  is given by the Fermi velocity obtained from the SdH oscillations. By assuming a simple spherical Fermi surface, we obtain  $v_F = \hbar k_F / m^* \approx 1.3 \times 10^4 \text{ m s}^{-1}$  from the SdH oscillations, where  $k_F \approx 1.7 \text{ nm}^{-1}$  is the Fermi wavenumber and  $m^* \approx 15 m_e$  is the effective mass<sup>25</sup>. We estimate  $\ell_{qp} \approx 54$  and 25 nm, which is nearly 70 and 30 times longer than the lattice constant, for crystals 1 and 3, respectively. Although the mean free path is long, the heavy effective mass leads to rather small mobilities: the mobility  $\mu = (e\ell_{qp}) / (m^* v_F)$  is about  $480 \text{ cm}^2 \text{ V}^{-1} \text{ s}^{-1}$  ( $0.048 \text{ T}^{-1}$ ) for crystal 1 and  $230 \text{ cm}^2 \text{ V}^{-1} \text{ s}^{-1}$  ( $0.023 \text{ T}^{-1}$ ) for crystal 3. This simple model explains why 30–40 T magnetic fields are needed to resolve the SdH oscillations and why the oscillations in crystal 3 are much smaller than those in crystal 1. Therefore, this rather crude estimate suggests that the enhanced thermal conductivity in zero field and the resistive QOs at high fields are intimately connected; that is, the long mean free paths imply that the neutral fermions are responsible for the QOs.

Very recently, a thermal Hall effect of neutral fermions that experience the Lorentz force, akin to the conduction electrons in metals, has been proposed<sup>16,42</sup>. In an attempt to observe such an effect, we measured the thermal Hall conductivity  $\kappa_{xy}$ . According to refs. <sup>16,42</sup>, the tangent of the thermal Hall angle

$$\tan \theta_H = \kappa_{xy} / \kappa_{xx} = \omega_c \tau \quad (2)$$

provides similar information on the electrical Hall angle in conventional metals<sup>36</sup>. Here,  $\omega_c = (eb)_{\text{eff}} / m^*$  corresponds to the cyclotron frequency of the neutral fermion, where  $b$  is the effective magnetic field experienced by neutral fermions, and  $\tau$  is the scattering time. Figure 4 depicts the field dependence of  $\omega_c^0 \tau \equiv \kappa_{xy}^0 / \kappa_{xx}^0$  at 0.2 and 0.5 K. As  $\kappa_{xx} > \kappa_{xx}^0$ ,  $\omega_c \tau$  is smaller than  $\omega_c^0 \tau$ . No discernible thermal Hall effect is observed;  $\omega_c^0 \tau$  and hence  $\omega_c \tau$  is less than 0.005 within our resolution. In conventional metals,  $\omega_c \tau = eB\tau / m^*$  becomes order of unity at the magnetic field where the QOs appear.

As the SdH oscillations are observed around 40 T (ref. <sup>25</sup>), the thermal Hall angle at 10 T could be expected to be of order 0.2, which is much larger than the observed thermal Hall angle. This suggests that  $(eb)_{\text{eff}}$  is significantly different from  $eB$  (see Methods)<sup>41,43</sup>. However, it is premature to conclude that the neutral fermions are not responsible for the SdH oscillations, because the small thermal Hall angle may be explained by a nonlinear  $B$  dependence of  $b$  or the presence of electron- and hole-like pockets of neutral fermions. In the latter scenario, compensation effects may reduce the thermal Hall signal considerably.

The presence of a Fermi surface of neutral fermions and the coupling to external magnetic field with negligible thermal Hall angle calls for further studies. The existence of the itinerant neutral fermions adds another piece to the puzzle of anomalous insulating states with metallic QOs.

## Online content

Any methods, additional references, Nature Research reporting summaries, source data, statements of code and data availability and associated accession codes are available at <https://doi.org/10.1038/s41567-019-0552-2>.

Received: 14 September 2018; Accepted: 12 May 2019;

Published online: 01 July 2019

## References

1. Tsunetsugu, H., Sigrist, M. & Ueda, M. The ground-state phase diagram of the one-dimensional Kondo lattice model. *Rev. Mod. Phys.* **69**, 809–863 (1997).
2. Riseborough, P. S. Heavy fermion semiconductors. *Adv. Phys.* **49**, 257–320 (2000).
3. Dzero, M., Sun, K., Galitski, V. & Coleman, P. Topological Kondo insulators. *Phys. Rev. Lett.* **104**, 106408 (2010).
4. Weng, H., Zhao, J., Wang, Z., Fang, Z. & Dai, X. Topological crystalline Kondo insulator in mixed valence ytterbium borides. *Phys. Rev. Lett.* **112**, 016403 (2014).
5. Xu, N. et al. Direct observation of the spin texture in SmB<sub>6</sub> as evidence of the topological Kondo insulator. *Nat. Commun.* **5**, 4566 (2014).
6. Hagiwara, K. et al. Surface Kondo effect and non-trivial metallic state of the Kondo insulator YbB<sub>12</sub>. *Nat. Commun.* **7**, 12690 (2016).
7. Li, G. et al. Two-dimensional Fermi surfaces in Kondo insulator SmB<sub>6</sub>. *Science* **346**, 1208–1212 (2014).
8. Tan, B. S. et al. Unconventional Fermi surface in an insulating state. *Science* **349**, 287–290 (2015).
9. Hartstein, M. et al. Fermi surface in the absence of a Fermi liquid in the Kondo insulator SmB<sub>6</sub>. *Nat. Phys.* **14**, 166–172 (2018).
10. Xiang, Z. et al. Bulk rotational symmetry breaking in Kondo insulator SmB<sub>6</sub>. *Phys. Rev. X* **7**, 031054 (2017).
11. Knolle, J. & Cooper, N. R. Quantum oscillations without a Fermi surface and the anomalous de Haas–van Alphen effect. *Phys. Rev. Lett.* **115**, 146401 (2015).
12. Knolle, J. & Cooper, N. R. Excitons in topological Kondo insulators: theory of thermodynamic and transport anomalies in SmB<sub>6</sub>. *Phys. Rev. Lett.* **118**, 096604 (2017).

13. Zhang, L., Song, X.-Y. & Wang, F. Quantum oscillation in narrow-gap topological insulators. *Phys. Rev. Lett.* **116**, 046404 (2016).
14. Baskaran, G. Majorana Fermi sea in insulating  $\text{SmB}_6$ : a proposal and a theory of quantum oscillation in Kondo insulators. Preprint at <https://arxiv.org/abs/1507.03477> (2015).
15. Erten, O., Chang, P.-Y., Coleman, P. & Tsvetkov, A. M. Skyrme insulators: insulators at the brink of superconductivity. *Phys. Rev. Lett.* **119**, 057603 (2017).
16. Chowdhury, D., Sodemann, I. & Sentil, T. Mixed-valence insulators with neutral Fermi-surfaces. *Nat. Commun.* **9**, 1766 (2018).
17. Sodemann, I., Chowdhury, D. & Sentil, T. Quantum oscillations in insulators with neutral Fermi surfaces. *Phys. Rev. B* **97**, 045152 (2018).
18. Shen, H. & Fu, L. Quantum oscillation from in-gap states and non-Hermitian Landau level problem. *Phys. Rev. Lett.* **121**, 026403 (2018).
19. Yoshida, T., Peters, R. & Kawakami, N. Non-Hermitian perspective of the band structure in heavy-fermion systems. *Phys. Rev. B* **98**, 035141 (2018).
20. Anderson, P. W., Halperin, B. I. & Varma, C. M. Anomalous low-temperature thermal properties of glasses and spin glasses. *Philos. Mag.* **25**, 1–9 (1972).
21. Matsuda, Y., Izawa, K. & Vechter, I. Nodal structure of unconventional superconductors probed by angle resolved thermal transport measurements. *J. Phys. Condens. Matter* **18**, R705–R752 (2006).
22. Xu, Y. et al. Bulk Fermi surface of charge-neutral excitations in  $\text{SmB}_6$  or not: a heat-transport study. *Phys. Rev. Lett.* **116**, 246403 (2016).
23. Boulanger, M.-E. et al. Field-dependent heat transport in the Kondo insulator  $\text{SmB}_6$ : phonons scattered by magnetic impurities. *Phys. Rev. B* **97**, 245141 (2018).
24. Fuhrman, W. T. et al. Interaction driven subgap spin exciton in the Kondo insulator  $\text{SmB}_6$ . *Phys. Rev. Lett.* **114**, 036401 (2015).
25. Xiang, Z. et al. Quantum oscillations of electrical resistivity in an insulator. *Science* **362**, 65–69 (2018).
26. Mignot, J.-M. et al. Evidence for short-range antiferromagnetic fluctuations in Kondo-insulating  $\text{YbB}_{12}$ . *Phys. Rev. Lett.* **94**, 247204 (2005).
27. Okawa, M. et al. Hybridization gap formation in the Kondo insulator  $\text{YbB}_{12}$  observed using time-resolved photoemission spectroscopy. *Phys. Rev. B* **92**, 161108(R) (2015).
28. Ikushima, K. et al.  $^{171}\text{Yb}$  NMR in the Kondo semiconductor  $\text{YbB}_{12}$ . *Physica B* **281–282**, 274–275 (2000).
29. Yamaguchi, J. et al. Kondo lattice effects and the collapse of lattice coherence in  $\text{Yb}_{1-x}\text{Lu}_x\text{B}_{12}$  studied by hard x-ray photoelectron spectroscopy. *Phys. Rev. B* **79**, 125121 (2009).
30. Utsumi, Y. et al. Bulk and surface electronic properties of  $\text{SmB}_6$ : a hard X-ray photoelectron spectroscopy study. *Phys. Rev. B* **96**, 155130 (2017).
31. Cooley, J. C., Aronson, M. C., Fisk, Z. & Canfield, P. C.  $\text{SmB}_6$ : Kondo insulator or exotic metal? *Phys. Rev. Lett.* **74**, 1629–1632 (1995).
32. Terashima, T. T. et al. Magnetization process of the Kondo insulator  $\text{YbB}_{12}$  in ultrahigh magnetic fields. *J. Phys. Soc. Jpn* **86**, 054710 (2017).
33. Nemkovski, K. S. et al. Lattice dynamics in the Kondo insulator  $\text{YbB}_{12}$ . *J. Solid State Chem.* **179**, 2895–2899 (2006).
34. Czopnik, A. et al. Low-temperature thermal properties of yttrium and lutetium dodecaborides. *J. Phys. Condens. Matter* **17**, 5971–5985 (2005).
35. Grechnev, G. E. et al. Electronic structure and bulk properties of  $\text{MB}_6$  and  $\text{MB}_{12}$  borides. *Low Temp. Phys.* **34**, 1167–1176 (2008).
36. Singleton, J. *Band Theory and Electronic Properties of Solids* (Oxford University Press, 2002).
37. Yamashita, M. et al. Highly mobile gapless excitations in a two-dimensional candidate quantum spin liquid. *Science* **328**, 1246–1248 (2010).
38. Yamashita, S., Yamamoto, T., Nakazawa, Y., Tamura, M. & Kato, R. Gapless spin liquid of an organic triangular compound evidenced by thermodynamic measurements. *Nat. Commun.* **2**, 275 (2011).
39. Watanabe, D. et al. Novel Pauli-paramagnetic quantum phase in a Mott insulator. *Nat. Commun.* **3**, 2082 (2012).
40. Balents, L. Spin liquids in frustrated magnets. *Nature* **464**, 199–208 (2010).
41. Motrunich, O. I. Orbital magnetic field effects in spin liquid with spinon Fermi sea: possible application to  $\kappa\text{-(ET)}_2\text{Cu}_2(\text{CN})_3$ . *Phys. Rev. B* **73**, 155115 (2006).
42. Katsura, H., Nagaosa, N. & Lee, P. A. Theory of the thermal Hall effect in quantum magnets. *Phys. Rev. Lett.* **104**, 066403 (2010).
43. Watanabe, D. et al. Emergence of nontrivial magnetic excitations in a spin-liquid state of kagomé volborthite. *Proc. Natl Acad. Sci. USA* **113**, 8653–8657 (2016).

## Acknowledgements

We thank K. Behnia, D. Chowdhury, P. Coleman, J. Knolle, H. v. Löhneysen, E.-G. Moon, R. Peters, S. Sebastian, T. Senthil and L. Taillefer for fruitful discussions. This work was supported by Grants-in-Aid for Scientific Research (KAKENHI) (nos. 25220710, 15H02106, 15H03688, 16K13837, 18H01177, 18H01180 and 18H05227) and on Innovative Areas 'Topological Material Science' (no. 15H05852) from the Japan Society for the Promotion of Science (JSPS). This work at Michigan is mainly supported by the Office of Naval Research through the Young Investigator Prize under Award No. N00014-15-1-2382 (electrical transport characterization), by the National Science Foundation under Award No. DMR-1707620 (magnetization measurement) and by the National Science Foundation Major Research Instrumentation award under No. DMR-1428226 (the equipment of the electrical transport characterizations). The development of the torque magnetometry technique in intense magnetic fields was supported by the Department of Energy under Award No. DE-SC0008110. A portion of this work was performed at the NHMFL, which is supported by National Science Foundation Cooperative Agreement No. DMR-1644779, the Department of Energy and the State of Florida. J.S. thanks the Department of Energy for support from the BES programme 'Science in 100 T'. The experiment at the NHMFL is funded in part by a QuantEmX grant from ICAM and the Gordon and Betty Moore Foundation through grant GBMF5305 to Z.X., T.A., L.C., C.T. and L.L. We are grateful for the assistance of T. Murphy, H. Baek, G. Jones, F. Balakirev, R. McDonald, J. Betts and J.-H. Park of the NHMFL.

## Author contributions

E.I. grew the high-quality single-crystalline samples. Y.S., Y.K., S.K. and H.M. performed the thermal transport measurements. T.T., S.K., O.T. and Y. Mizukami performed the heat capacity measurements. Z.X., L.C., T.A., C.T., J.S. and L.L. performed the high-field resistivity measurements. Y.S., Z.X., Y.K., T.T., S.K., H.M., Y. Mizukami, T.S., L.L. and Y. Matsuda analysed the data. Y.S., Y.K., T.S., J.S., L.L. and Y. Matsuda prepared the manuscript.

## Competing interests

The authors declare no competing interests.

## Additional information

**Supplementary information** is available for this paper at <https://doi.org/10.1038/s41567-019-0552-2>.

**Reprints and permissions information** is available at [www.nature.com/reprints](http://www.nature.com/reprints).

**Correspondence and requests for materials** should be addressed to L.L. or Y. Matsuda

**Publisher's note:** Springer Nature remains neutral with regard to jurisdictional claims in published maps and institutional affiliations.

© The Author(s), under exclusive licence to Springer Nature Limited 2019

## Methods

**Crystal growth and sample preparation.** YbB<sub>12</sub> single crystals were grown by the travelling-solvent floating-zone method<sup>44</sup>. Three crystals (1, 2 and 3) were cut from the as-grown ingot and polished into a rectangular shape. Crystals 1 and 2 were taken from the same growth batch and crystal 3 was from a different growth batch. The dimensions of the samples were 4.0 × 0.52 × 0.51 mm<sup>3</sup> (crystal 1), 1.0 × 1.0 × 0.2 mm<sup>3</sup> (crystal 2) and 1.8 × 0.81 × 0.13 mm<sup>3</sup> (crystal 3). Crystals 1, 2 and 3 correspond to sample N3, N1 and N4 in ref.<sup>25</sup>, respectively.

**High-field resistivity measurements.** The magnetoresistivities of YbB<sub>12</sub> crystals 1, 2 and 3 were measured in a capacitor-driven 65 T pulsed magnet at the National High Magnetic Field Laboratory (NHMFL), Los Alamos. A low environment temperature was achieved by using a <sup>3</sup>He cryostat. For the different probes we used, the base temperature varied: 0.69 K for crystals 1 and 2 and 0.53 K for crystal 3. Magnetic field was applied parallel to one of the cubic axes. An offset of a few degrees was expected due to the misalignment in sample mounting. Considering the different sizes and geometries of the samples, we measured the magnetoresistivity with the current parallel to the magnetic field (**I**||**B**) in crystal 1, and **I**⊥**B** in crystals 2 and 3. For all three crystals, we used a standard four-contact configuration and the magnetoresistivity data were taken via a high-frequency a.c. technique<sup>45</sup> with a specialized digital lock-in programme. The driving signal (*f* = 192 kHz for crystals 2 and 3, and 256 kHz for crystal 1) was generated by an a.c. voltage source and applied to the sample across a transformer. The current through the sample was monitored using a 10 Ω shunt resistor, and was determined to be 38–66 μA in our experiment.

**Heat capacity measurements.** The heat capacity was measured down to *T* ~ 0.6 K by a long-relaxation calorimetry using a bare chip resistance thermometer (Cernox 1030BR, Lakeshore)<sup>46</sup>, which enabled very small addenda contribution to the total heat capacity. The heat capacity of the addenda including the grease was measured before the sample was mounted. The temperature dependence of the addenda was fitted by a polynomial function and subtracted from the total heat capacity. The obtained heat capacity was analysed as a sum of the phonon, quasiparticle and Schottky contributions,  $C = C_{\text{ph}} + C_{\text{qp}} + C_{\text{sc}}$  (see Supplementary Fig. 4 and Methods).

**Thermal and thermal Hall conductivity measurements.** The longitudinal and transverse thermal conductivities,  $\kappa_{xx}$  and  $\kappa_{xy}$ , were measured by the steady-state method, applying the thermal current **q** with **q**||**x** [100] and **H**||**z** [001]. The thermal gradients  $-\nabla_x T$ ||**x** and  $-\nabla_y T$ ||**y** were detected by RuO<sub>2</sub> thermometers, and  $\kappa_{xx} = w_{xx}/(w_{xx}^2 + w_{xy}^2)$  and  $\kappa_{xy} = w_{xy}/(w_{xx}^2 + w_{xy}^2)$  were obtained from the thermal resistivity  $w_{xx} = \nabla_x T/q$  and thermal Hall resistivity  $w_{xy} = \nabla_y T/q$ . The effect of misalignment of the Hall contacts was eliminated by reversing the magnetic field at each temperature.

**Equilibrium conditions.** In the thermal conductivity measurements, we always measured the time *t* dependence of  $\Delta T_x(t) = T_1 - T_0$ , the temperature difference between two contacts, after a constant heat pulse (power *P*) is applied (see Supplementary Fig. 2a for the experimental set-up). Supplementary Fig. 2b shows  $\Delta T_x(t)$  at 0.4 K. After the heater power is turned on,  $\Delta T_x(t)$  increases as  $\Delta T_x(t) = D[1 - \exp(-t/\tau)]$ , where  $\tau$  is the relaxation time, which is the order of 1 min at 0.4 K. As shown in Supplementary Fig. 2b,  $\Delta T_x(t)$  becomes constant at *t* >  $\tau$ . We confirmed that no deviation from the constant value is observed for more than 4 h at 0.8 K ( $|\Delta T_x(t) - D|/D < 0.01$  at *t* > 3 min) (Supplementary Fig. 2c). Similar results were obtained at 0.3 K and 2 K. As shown in Supplementary Fig. 2b and its inset, we also always checked the linearity of  $\Delta T_x$  and *P*. Thus, in the timescale of the measurements, we confirmed that the system is in thermal equilibrium.

As for the SdH oscillation experiments, we measured the resistivity by using an a.c. technique with *f* > 100 kHz in pulsed fields at fixed temperatures. The observed oscillation frequencies are close to the previously reported values<sup>25</sup>, where SdH oscillations were measured with *f* = 7–20 Hz in static magnetic fields. These results indicate that the SdH effect is intrinsic and reflects the electronic structure of a thermal equilibrium system in YbB<sub>12</sub>.

**Longitudinal and transverse thermal conductivities.** Supplementary Fig. 3a,b displays the temperature dependence of the longitudinal thermal conductivity  $\kappa_{xx}/T$  for crystals 1 and 3, respectively. The linear temperature term of  $\kappa_{xx}$  in the zero-temperature limit,  $\kappa_{xx}^0/T$ , is obtained by extrapolating  $\kappa_{xx}/T$  at each field. The field dependence of  $\kappa_{xx}^0/T$  is shown in Fig. 3c. The thermal Hall angle  $\tan\theta_{\text{H}} = \kappa_{xy}/\kappa_{xx}^0$  is obtained from  $\kappa_{xx}^0/T$  in Fig. 3c and  $\kappa_{xy}/T$  in Supplementary Fig. 3c.

**Analysis of heat capacity.** The temperature dependence of the heat capacity is analysed as a sum of the phonon, quasiparticle and Schottky contributions,  $C = C_{\text{ph}} + C_{\text{qp}} + C_{\text{sc}}$ , where

$$C_{\text{qp}} = \gamma T$$

$$C_{\text{ph}} = \beta T^3 + \frac{A_1}{T} \left( \frac{\Theta_{\text{E1}}}{T} \right)^2 \frac{\exp(\Theta_{\text{E1}}/T)}{[\exp(\Theta_{\text{E1}}/T) - 1]^2} + \frac{A_2}{T} \left( \frac{\Theta_{\text{E2}}}{T} \right)^2 \frac{\exp(\Theta_{\text{E2}}/T)}{[\exp(\Theta_{\text{E2}}/T) - 1]^2}$$

$$C_{\text{sc}} = \frac{B}{T^2} \left\{ \frac{\sum_{i=0}^{n-1} \Delta_i \exp(-\Delta_i/T)}{\sum_{i=0}^{n-1} \exp(-\Delta_i/T)} - \left( \frac{\sum_{i=0}^{n-1} \Delta_i \exp(-\Delta_i/T)}{\sum_{i=0}^{n-1} \exp(-\Delta_i/T)} \right)^2 \right\}$$

Here,  $C_{\text{ph}}$  includes Debye and Einstein contributions with two optical phonon modes, and the Schottky contribution is obtained from a three-level model with  $n = 3$  and excitation energies  $\Delta_i$ , where  $\Delta_0 = 0$ . The best fit yields  $\gamma = 3.8 \text{ mJ mol}^{-1} \text{ K}^{-2}$ ,  $\beta = 0.026 \text{ mJ mol}^{-1} \text{ K}^{-4}$ ,  $\Theta_{\text{E1}} = 16 \text{ K}$  and  $\Theta_{\text{E2}} = 170 \text{ K}$  for crystal 2 and  $\gamma = 3.8 \text{ mJ mol}^{-1} \text{ K}^{-2}$ ,  $\beta = 0.017 \text{ mJ mol}^{-1} \text{ K}^{-4}$ ,  $\Theta_{\text{E1}} = 24 \text{ K}$  and  $\Theta_{\text{E2}} = 160 \text{ K}$  for crystal 3 in zero field (Supplementary Fig. 4a,b). Supplementary Fig. 4c,d shows the field dependence of the coefficients of the three-level Schottky contribution,  $\Delta_1$ ,  $\Delta_2$  and *B* for crystals 2 and 3, respectively.

**Magnetic susceptibility.** The magnetic susceptibility  $\chi$  of the YbB<sub>12</sub> single crystals used for the heat capacity and thermal conductivity measurements was measured by a Quantum Design VSM magnetometer. Supporting high-field magnetization was measured with torque magnetometry in intense magnetic fields at the NHMFL. Supplementary Fig. 5 shows the temperature dependence of  $\chi$  measured at 1 T for crystals 2 and 3. The Curie contribution at low temperature is very small compared to that in the previous report<sup>47</sup>, indicating high quality of the present crystals.

**Estimation of the effective Lorentz force on the charge-neutral fermionic excitations.** Using equation (2), the ratio of the Lorentz force acting on the charge-neutral excitations and that on electrons,  $|(eb)_{\text{eff}}/(eB)_e|$ , is estimated as

$$\frac{(eb)_{\text{eff}}}{(eB)_e} = \omega_c \tau \frac{m^*}{\tau(eB)_e}$$

where  $\omega_c = (eb)_{\text{eff}}/m^*$ .  $m^* = 15m_e$  is the effective mass determined by the SdH oscillations and  $\tau = \ell/v_F \approx \frac{54 \text{ nm}}{3 \times 10^8 \text{ m s}^{-1}} \approx 4.2 \times 10^{-12} \text{ s}$  and is the scattering time of the neutral excitations estimated from  $\kappa_{xx}^0/T$  and  $\gamma$  (see the main text). As shown in Fig. 4,  $\omega_c \tau < 0.005$  at 12 T. We obtained  $|(eb)_{\text{eff}}/(eB)_e| < 0.1$ . Although this simple estimation should be scrutinized, it suggests that the Lorentz force acting on the neutral excitations is very weak below 12 T.

**Low-dimensional phonons.** Although the isotropic 3D phonon structure is firmly confirmed in YbB<sub>12</sub> with cubic structure, here we discuss the contribution of low-dimensional phonons to  $\kappa_{xx}$ . In 1D materials such as silicon nanowires, linear *T*-dependence of  $\kappa_{xx}$  has been observed, suggesting a significant role of 1D phonons. However, such linear *T*-dependence is observed above *T* ≈ 30 K (ref.<sup>48</sup>), which is far above the temperature range of the present study. A recent study on silicon nitride nanowires has revealed that  $\kappa_{xx}$  does show linear *T*-dependence but shows *T*<sup>2</sup> dependence at very low temperature down to 0.1 K (ref.<sup>49</sup>). Thus, there is no reason to attribute the linear low-temperature thermal conductivity observed in YbB<sub>12</sub> to the 1D phonons.

## Data availability

The data that support the plots within this paper and other findings of this study are available from the corresponding authors upon reasonable request.

## References

- Iga, F., Shimizu, N. & Takabatake, T. Single crystal growth and physical properties of Kondo insulator YbB<sub>12</sub>. *J. Magn. Magn. Mater.* **177–181**, 337–338 (1998).
- Kohama, Y., Marcenat, C., Klein, T. & Jaime, M. AC measurement of heat capacity and magnetocaloric effect for pulsed magnetic fields. *Rev. Sci. Instrum.* **81**, 104902 (2010).
- Taylor, O. J., Carrington, A. & Schlueter, J. A. Specific-heat measurements of the gap structure of the organic superconductors  $\kappa$ -(ET)<sub>2</sub>Cu[N(CN)<sub>2</sub>]Br and  $\kappa$ -(ET)<sub>2</sub>Cu(NCS)<sub>2</sub>. *Phys. Rev. Lett.* **99**, 057001 (2007).
- Iga, F. et al. Kondo-semiconductor to Kondo-impurity transition in the heat capacity of Yb<sub>1-x</sub>Lu<sub>x</sub>B<sub>12</sub>. *Physica B* **259–261**, 312–314 (1999).
- Li, D. et al. Thermal conductivity of individual silicon nanowires. *Appl. Phys. Lett.* **83**, 2934–2936 (2003).
- Tavakoli, A. et al. Universality of thermal transport in amorphous nanowires at low temperatures. *Phys. Rev. B* **95**, 165411 (2017).